Hydrol. Earth Syst. Sci. Discuss., 9, 3691–3720, 2012
www.hydrol-earth-syst-sci-discuss.net/9/3691/2012/
doi:10.5194/hessd-9-3691-2012

Hydrology and Earth System Sciences Discussions

Ground-penetrating radar insight into a coastal aquifer: the freshwater lens of Borkum Island

J. Igel[1], **T. Günther**[1], **and M. Kuntzer**[2]

[1]Leibniz Institute for Applied Geophysics (LIAG), Hannover, Germany
[2]Institute for Soil Science, Leibniz University Hannover, Hannover, Germany

Received: 2 March 2012 – Accepted: 8 March 2012 – Published: 16 March 2012

Correspondence to: J. Igel (jan.igel@liag-hannover.de)

Published by Copernicus Publications on behalf of the European Geosciences Union.

Abstract

Freshwater lenses within islands are an important resource for drinking water. The aim of the GPR investigation was to map the shape of the groundwater table and sedimentary structures on Borkum island as input parameters for hydrogeological simulation.

In total, 20 km of constant offset (CO) radar profiles were measured with centre frequencies of 80 and 200 MHz. Wave velocities were determined by common midpoint (CMP) measurements and vertical radar profiling (VRP) in a monitoring well. The 80 MHz CO data show a clear reflection at the groundwater table, whereas the reflection is blurry and shifted to lower frequencies for the 200 MHz data. This is caused by the gradual increase of water content above the capillary fringe. The GPR-derived water tables are in good accordance with the observation of the monitoring wells in the area. In the centre of the island, the groundwater table is found up to 3.5 m above sea level, however it is lower towards the coast line. Some local depressions are observed in the region of dune valleys and around pumping stations of the local water supplier. GPR also reveals details within the sediments and highly-permeable aeolian sands can be distinguished from less-permeable marine sediments. A sharp horizontal reflection below the water table can be seen on many profiles and is identified as a hydraulically-tight silt loam layer by hand-drilled boreholes. Moreover, GPR data indicate scattered erosion channels in this layer that cause it to be an aquitard with some leakage.

GPR provides a high resolution map of the groundwater table and insight into the stratigraphy of the sediments that are a valuable complementary information to the observation of monitoring wells.

1 Introduction

Borkum is the largest and westernmost island of the East Frisian islands chain along the German North Sea coast. It covers an area of 31 km^2 and is located 10 km north

HESSD

9, 3691–3720, 2012

of the mainland. It is a typical barrier island with dunes at the northern open sea side and a low marshland at the southern land side.

When rainwater seeps through the ground surface of an island, it cumulates in the subsurface. Due to its lower density, the freshwater floats on top of the saltwater and forms a freshwater lens analogous to an iceberg floating in the sea. Only a small part of the freshwater lens emerges above the sea level whereas the larger part is below. The correlation between the thickness of the freshwater lens and the height of the groundwater table above sea level was first observed and described by Ghyben and Herzberg (Herzberg, 1901):

$$h = \frac{\rho_s - \rho_f}{\rho_f} z, \tag{1}$$

where h is the height of the groundwater table above sea level (a.s.l.), z the thickness of the freshwater lens below sea level, and $\rho_s = 1.025\,\mathrm{g\,cm^{-3}}$ and $\rho_f = 1\,\mathrm{g\,cm^{-3}}$ the density of salt- and freshwater, respectively. When using these values (Eq. 1) leads to $z = 40h$. However, this relationship is only valid for a homogeneous halfspace and stationary conditions.

Within the CLIWAT project (CLImate and groundWATer), the impact of climate change and seawater rise on freshwater resources of coastal aquifers is investigated by long-term hydraulic simulations. The island of Borkum was one of the pilot areas that was intensely investigated. Hydrogeologic models are usually founded on general geologic information, drill cores, monitoring wells, and pumping tests. Besides, a variety of geophysical techniques were evaluated within the CLIWAT project with regard to their capability to give further valuable information on large areas like hydraulically relevant subsurface structures, hydraulic properties and the shape of the freshwater lens. The geophysical techniques include seismics, airborne electromagnetics (Siemon et al., 2009), electric restivity tomography (ERT) from the surface as well as in boreholes (Grinat et al., 2010), magnetic resonance soundings (MRS) (Günther and Müller-Petke, 2012), direct push techniques, and ground-penetrating radar (GPR).

HESSD
9, 3691–3720, 2012

The aim of this paper is to evaluate the capability of GPR to investigate the near-surface aquifer of Borkum island and to demonstrate the benefit of GPR investigation as a part of geophysical exploration for realistic hydraulic simulation of future developments of an island freshwater lens (Sulzbacher et al., 2012). The main targets of interest are the groundwater table of the freshwater lens and clayey/silty layers in the sandy sediments acting as aquitards.

Ground-penetrating radar has shown to be a powerful tool for environmental and hydrogeologic investigations in particular in rocks and sediments with low electric conductivity. It is successfully used for high resolution investigations in sedimentology and landform characterisation (Bristow et al., 2000; Neal, 2004; van Dam, 2012) and showed to be an outstanding tool for mapping large-scale architecture and small-scale internal structures in coastal barriers (Møller and Anthony, 2003; Nielsen et al., 2009; Bennett et al., 2009). GPR has also proven its ability to detect groundwater tables in sandy aquifers (Harari, 1996; Doolittle et al., 2006; Rejiba et al., 2012). Tronicke et al. (1999) investigated the freshwater lens of a barrier island by a combination of electric resistivity soundings and GPR. They constructed a groundwater contour map for the hole island of Spiekeroog from observation wells and GPR at single points where the groundwater table was clearly identifiable and the height of the ground surface was known. Kruse et al. (2000) investigated a very thin (1–1.5 m) freshwater lens on Key Largo, Florida, with GPR and obtained a strong water table reflection followed by a weak reflection from the transition zone from fresh- to saltwater below.

2 GPR investigations

2.1 Velocity determination

An essential step of every GPR survey is to determine the radar-wave velocities in the subsurface. As in seismics, the velocity is needed to transform traveltimes into depths and a good velocity model is fundamentally important to deduce a quantitative

HESSD
9, 3691–3720, 2012

structural map of the underground. Radar velocities v depend on dielectric permittivity ε_r and for low-loss materials this relation is given by:

$$v = \frac{c}{\sqrt{\varepsilon_r}}, \tag{2}$$

where c is the speed of light. Permittivity is linked to further material properties as primarily water content and porosity and to a lower degree the mineral composition of the grains (e.g., Topp et al., 1980). One often used formula is based on the complex refractive index method (CRIM). It relates the volumetric fractions of the sediment compounds, the solid matrix, the water and air that fill the pore space and their particular permittivities to the bulk permittivity of the mixture (Shen et al., 1985):

$$\sqrt{\varepsilon_r^{\text{bulk}}} = (1 - \Phi)\sqrt{\varepsilon_r^{\text{m}}} + \theta_V \sqrt{\varepsilon_r^{\text{w}}} + (\Phi - \theta_V)\sqrt{\varepsilon_r^{\text{a}}}. \tag{3}$$

Φ is the porosity, θ_V the water content and ε_r^{m}, ε_r^{w}, and $\varepsilon_r^{\text{a}} = 1$ are the permittivities of matrix, water, and air, respectively. Thus, reliable velocity values can be used to characterise rocks and sediments and to deduce hydraulically relevant properties: porosity and water content.

Two techniques were used in this study to assess wave velocities that originally stem from seismics but had been adapted to GPR.

2.1.1 CMP soundings

Common midpoint (CMP) measurements are a common tool to deduce wave velocities in the subsurface. In case of GPR, transmitter and receiver antenna are stepwise separated from a constant midpoint and at each distance a trace is recorded (e.g., Annan, 2005). The shape of reflection hyperbolas depends on the mean radar velocity above the reflector. In case of an adequate number of reflectors in the subsurface, the interval velocities in between these reflectors can be calculated and a velocity-depth model can be deduced.

HESSD
9, 3691–3720, 2012

A couple of CMP measurements were carried out in the area of the GPR investigations. Figure 1b shows an example acquired with unshielded 80 MHz antennas (GSSI MLF antenna) on top of a dune with an antenna offset of 1–39 m and 0.5 m intervals. Static correction and amplitude balancing (removal of header gain and divergence compensation) has been performed. The air wave can clearly be recognised as primary onset in the radar section followed by critically refracted waves, the ground wave and several reflected waves. Figure 1c shows the results of a semblance analysis that is used to find the mean velocity and traveltime of reflections in the radar section. The energy along calculated reflection hyperbolas is summed up for every combination of traveltime and mean velocity and a reflection at a plain surface is focused to a point in the semblance plot (Yilmaz, 2001). The air wave appears as an energy maximum at $t = 0$ ns and $v = 0.3\,\mathrm{m\,ns^{-1}}$ and reflected waves appear at longer traveltimes and lower mean velocities. The fine tuning of velocity determination was done by interactively adapting the calculated reflection hyperbolas to the first onsets in the radar section (red curves in Fig. 1b). A velocity-depth-model is then calculated by using the Dix-formula (Dix, 1955) and by transforming the mean velocities to interval velocities in between the reflectors (Fig. 1a). The velocity is quite constant at $0.125\,\mathrm{m\,ns^{-1}}$ for the shallow subsurface representing the unsaturated zone. At approx. 200 ns the velocity shows a steep decrease to $0.065\,\mathrm{m\,ns^{-1}}$ which corresponds to the water saturated sand below the groundwater table. The CMPs at the other locations show quite similar results with velocities of 0.125 and $0.065\,\mathrm{m\,ns^{-1}}$ for the unsaturated and saturated sand, respectively, differing by ±10 %.

CMP soundings have the advantage that they do not need any well and can be carried out at favoured locations in an area. However, the drawback is they can only provide velocities in between distinct reflectors, i.e. the vertical resolution may be quite bad depending on geology.

HESSD
9, 3691–3720, 2012

2.1.2 VRP soundings

Subsurface radar velocities can be very accurately determined by GPR borehole measurements as the propagation path of the waves is a priori known. Tomographic cross-hole measurements can provide detailed subsurface models (e.g. Tronicke et al., 2004; Ernst et al., 2007; Klotzsche et al., 2010). However, this method requires a significant effort and at least two boreholes at a very short distance, which is rarely found in the field. Vertical radar profiling (VRP) needs only one borehole, e.g. every groundwater monitoring well in which a borehole antenna fits ($\geq 2''$) can be used as long as plastic tubes were installed. One antenna is lowered in the borehole and the other antenna is placed at the ground surface. It is similar to vertical seismic profiling (VSP) that is a well-established technique for deducing seismic velocity models (Hardage, 2000). In hydrogeophysics, VRP has successfully been used, e.g. to obtain a moisture content profile in a landfill to assess its capping effectiveness (Cassiani et al., 2008).

Vertical radar profiling measurements were carried out in two monitoring wells located on top of a dune and in a dune valley. A Malå RAMAC 100 MHz slimhole receiver was placed in the borehole and a 100 MHz unshielded surface transmitter was placed at different offsets from the hole in radial polarisation direction. At every transmitter offset, the receiver was lowered down the borehole and a trace was recorded every 10 cm.

Besides direct waves that propagate on the shortest way from the transmitter to the receiver, refracted waves may occur that first propagate through air to the borehole and then down to the receiver. For larger offsets, these waves are faster than the direct wave and cause interferences, wherefore near-offset transmitter positions are preferred (Tronicke and Knoll, 2005). On the other hand, short offsets result in weak radar amplitudes due to the different polarisation of surface and borehole antenna and the resulting radiation pattern. When assuming ideal infinitesimal dipoles, the simple multiplication of the radiation pattern of the co-polarised transmitting and receiving antenna results in a very poor sensitivity for small offsets and weak radar amplitudes are

HESSD
9, 3691–3720, 2012

expected. Thus, there is a trade-off between the requirement to avoid waves critically refracted at the earth's surface and the quest to record high amplitude data (Tronicke and Knoll, 2005). However, real borehole antennas are not ideal dipoles and still have a considerable sensitivity in dipole direction and we could not observe a significant rise in amplitudes with increasing transmitter offset. Thus, we used an offset of 1 m, which showed the best data quality for further analysis.

A dewow-filter was applied (10 ns running mean) in order to remove low frequency noise and the traces were normalised (Fig. 2). The first arrival times were picked and inverted using a smoothness-constrained Gauss-Newton algorithm similar to Clement and Knoll (2006). Straight rays between transmitter and receiver were assumed. Regularisation strength was subsequently reduced and the roughness of the velocity curve was iteratively used as weighting factor in order to achieve sharp contrasts, e.g. at the groundwater table (Fig. 3). The model shows a sharp decrease of radar velocity at the groundwater table with a quite homogeneous velocity of 0.121–0.132 m ns^{-1} in the unsaturated zone above and 0.064–0.065 m ns^{-1} in the saturated zone below. The groundwater table in the monitoring well was measured with a light plummet and is plotted in Fig. 3 as well as the top of the capillary fringe that has been experimentally determined (see Sect. 3).

2.2 CO profile measurements

About 20 km of GPR profiles in a constant-offset setup were acquired in the eastern part of the island by using a GSSI SIR 3000 with 80 MHz unshielded and 200 MHz shielded antennas with an offset of 2 and 0.3 m and trace increments of 0.1 and 0.05 m, respectively (see Fig. 10). Due to the dense vegetation and regulations of the nature protection area, the survey was limited to roads, gravel paths and trails. The exact antenna position and the elevation were tracked by a Trimble 5800 differential global positioning system (DGPS) with base station on the island yielding an accuracy of approx. 1 cm for the position and 5 cm for the absolute elevation. At a few locations no DGPS signal was available due to interruptions in either communication to the base

HESSD
9, 3691–3720, 2012

station or to satellites and the radar data were not used for analysis. Further, some sections of the radar profiles were highly disturbed by antenna ringing so that no geologic structures could be identified. The ringing was caused either by an electrically conductive ground of the lower marshland that is flooded by seawater from time to time, or by metal installations in the subsurface. Such installations were water pipes, cables, remains of a railway track and in some parts the reinforcement of the road concrete pavement. However, most of the radar sections showed good data quality with investigation depths of up to 10 m.

Figure 4 shows a GPR section measured from the North Sea over the main dune area in direction of the inner island using two different antennas (profile 1, Fig. 10). Time-zero was corrected and gain balancing was performed to remove the time-dependent gain of the GPR device and counterbalance for spherical spreading. A dewow filter (5 and 20 ns running mean) was applied to remove low frequency noise. In addition, the 80 MHz data were lowpass filtered (120/240 MHz) to remove high frequency noise. Topographic correction was done on the basis of the DGPS elevations and the mean velocity of the unsaturated zone was used to deduce the correction times from the elevations. The non-linear depth axis is calculated using the mean velocities of the unsaturated and saturated zone, i.e. v = 0.124 and 0.065 m ns^{-1}, respectively and the position of the mean sea level (m.s.l.) is marked on the axis. Horizontal reverberations in the 80 MHz data following the topography were not removed by $f-k$-filtering or background removal because this would also extenuate the generally horizontal groundwater reflection as well as horizontal geological reflections. A migration of data was not necessary as the reflections were not steep (note that the radar sections are highly exaggerated). Penetration depth is poor and antenna ringing is strong on the most northern part of the profile on the beach. This is caused by the high electrical conductivity of the saltwater saturated sand. When going south over the dune data quality is very good with penetration depths of 10 m and more. The 80 MHz data with unshielded antennas show some steeply inclined surface reflections that probably stem from a fence on top of the dune. The groundwater table can be recognised as

HESSD
9, 3691–3720, 2012

an almost horizontal reflection at a depth of 10 m below the maximum elevation of the dune. Above the groundwater table, the radar reflections are caused by stratigraphic boundaries within the dune. The 200 MHz data provide a very detailed structural map of the dune sedimentation.

A radar section (200 MHz) of the inner dune region is shown in Fig. 5 (profile 2, Fig. 10). In the upper part cross stratification is dominant whereas in the lower part the stratigraphy is almost horizontal. A strong reflector follows roughly the topography and is elevated up to 1 m in the centre of the profile and descends to both sides. Further, a sharp dominant reflection can be seen at a depth of 6 m below the highest elevation of the profile.

Figure 6 shows a detail of the section. In addition, the data have been migrated (Fig. 6b) by an FD algorithm using a 2-D velocity model (Sandmeier, 2011). The migration does not change the inclination of the cross bedding structures as they are relatively flat (note the exaggeration) but focuses back the diffraction hyperbolas, e.g. at the discontinuities of the sharp reflector at 6 m depth so that these structures can be interpreted.

3 Geology and sampling

The geology of the island is based on the interaction of tidal and climatic sea level variation and a prevailing western wind direction. The underground of the island is build by Holocene sandy sediments. Primarily, it was an alluvial formation deposited by the sea. Its topography was formed by the wind, causing the development of dunes. The deposits consist predominantly of quartz sands with interfered layers of peat, clay, silt and shell detritus in places. The basis of these formations is situated at approx. 20 m b.s.l. and consist of glacial sediments from the Pleistocene period (Keilhack and Wildvang, 1925).

In addition to near-surface auger sampling, 3 boreholes along GPR profile 2 were driven by hand to a maximum depth of 6 m by using a drill hammer (see Figs. 5 and

HESSD
9, 3691–3720, 2012

7). The humous topsoil and the slightly humous subsoil have a thickness of 10 and 30 cm, respectively. Further down the sediments consist of moderately calcareous fine-medium sands. They are crossed by several layers with different organic matter content and a 0.1 m thick peat layer. The sediments above and below the groundwater fluctuation zone show different colours caused by the varying redox potentials in the oxidizing and the reducing environment. In larger depth the fine-medium grained sand is loaded with shell detritus overlying a 0.2–0.3 m thick layer of silt loam with a high content of organic matter. Within these loamy deposits that represent the former surface of the tidal flat, small layers of fine-medium sand are included in places. Below this layer the fine-medium sand is silty and enriched with shell detritus and interspersed clay layers.

The grain-size distribution of the drill core samples were analysed by a Beckman Coulter LS 13320 laser diffractometer. Characteristic samples for each sedimentological block are plotted in Fig. 8. The sediments of the upper drill core are well sorted and rounded, as identified by microscopic analysis (sample B1 and B4). These sediments are aeolian dune sands that are characterized by accumulation layers as found in the drill cores. The marine sediments directly above and below the silty loam layer (B8) are not sorted that good and have a 20 % silt fraction (B9). Grain densities and porosity of the dune sands were determined to 2.66 g cm^{-3} and 39–42.5 % with a Quantachrome pycnometer for disturbed and loosely packed samples. Further, the capillary rise height of the sand was experimentally determined. The dry sand was filled into a tube and put into a water basin and the rise height was observed with time. After 3 days the height was at 13.5 cm above the water table and did not change any more. Electric bulk conductivity was also determined for some water saturated samples and was 0.008 S m^{-1} for the aeolian sand (B4), 0.037 S m^{-1} for the peat (B2), and 0.077 S m^{-1} for the silty loam (B8).

HESSD
9, 3691–3720, 2012

4 Results and interpretation

4.1 GPR velocities and hydraulic properties

Mean radar velocities were determined by CMP and VRP analysis to 0.124 and 0.065 m ns^{-1} in the unsaturated and saturated zone corresponding to permittivities of ε_r = 5.9 and ε_r = 21.6, respectively (Eq. 2). The values are in good agreement to common radar velocities in similar environments (Møller and Anthony, 2003).

The CRIM formula (Eq. 3) was used to derive the porosity from the bulk permittivity of the saturated zone for which $\theta_V = \Phi$. For this, the permittivity of the matrix was set to the permittivity of quartz ($\varepsilon_r^{\mathrm{m}}$ = 4.6) and the permittivity of water to $\varepsilon_r^{\mathrm{w}}$ = 84.0, which is the value at 10 °C and 100 MHz (Kaatze, 1989). This results in a porosity of Φ = 35.6 % that corresponds very well to literature values for a compacted fine to medium sand (Φ = 35 %, Ad-hoc-AG Boden, 2005). The porosities of the sand determined with a pycnometer (39–42.5 %) were higher as disturbed and only slightly compacted samples were used. The water content of the unsaturated zone was calculated in a second step by using the deduced porosity to θ_V = 8 %, which is a little bit less than the field capacity of a fine to medium sand (Ad-hoc-AG Boden, 2005).

4.2 Sedimentological structures

In the GPR sections Figs. 4–6 a variety of reflections can be seen that originate from sedimentological interfaces. They comprise clay, loam and peat layers as well as slight changes in the grain-size distribution, compaction and organic content of the sand in the dune body. These small changes can often hardly be detected in core samples, however, they cause changes in water content and thus dielectric permittivity and yield distinct radar reflections. In Figs. 5 and 6 we can distinguish an area above 5 m depth with predominantly cross bedding structures that are typical for aeolian sedimentation. Below, layering is horizontal and the material is interpreted as marine deposit. This is in good agreement with the core samples that show shell detritus in this deeper

HESSD
9, 3691–3720, 2012

area. Further, when looking at the grain-size distributions, the sediments above 5 m are well sorted and the sediments below are less sorted. The distinct reflector at 6 m can be correlated to a silt loam layer with high electric conductivity and is interpreted as a former tidal flat surface that hydraulically acts as an aquitard. A detailed look at this structure (Fig. 6) shows discontinuities causing diffractions in the unmigrated GPR data. In the migrated data, the discontinuities can be interpreted as erosion channels of the former tideways. These structures are a few decimeters to meters wide and up to 40 cm deep so that the layer is likely to show some leakage to water flow. This finding is confirmed by pumping tests that were carried out all over the island (Sulzbacher et al., 2012) where in some areas this layer separates the upper unconfined aquifer from a lower confined aquifer and in other areas they could not be distinguished.

The reflection from the silt loam was detectable in most radar profiles in an area of approx. 1 km^2 in the centre part of the investigation area. The onsets were picked and the traveltimes transformed into depth by using the correct radar velocities and DGPS elevations (Fig. 9). The layer shows some topography and is located at about 0 m a.s.l.

4.3 Groundwater table of the freshwater lens

The groundwater table causes a strong reflection due to the high contrast in dielectric permittivity and can be seen in Figs. 4–6. The groundwater reflection appears stronger in the low frequency data than in the high frequency data (see Fig. 4) and is shifted to lower frequencies compared to geological reflections. The reason for this is the gradual increase of water content (and permittivity) in the transition zone above the groundwater table (Harari, 1996) that causes a frequency-dependent reflection coefficient. The lower the frequency, i.e. the longer the wavelength, the sharper is the contrast for the waves and the stronger is the reflection. On the other hand, the resolution is worse for the 80 MHz data. Further, for shallow groundwater tables, the reflection was masked by the primary wavelet for this antenna. Thus, a combination of both antennas showed to be a flexible way to map the groundwater table with changing coverage height of dune sediments. The groundwater table is low near the coast and rises towards the

HESSD
9, 3691–3720, 2012

inner dune part of the island (Fig. 4). The GPR section in the central area of the island (Fig. 5) shows a curved groundwater table. It is about 1 m higher in the centre of the profile and sinks down to both sides where the land surface is lower.

The groundwater table was picked in the sections where clearly visible, i.e. on profiles with good data quality and when the coverage was not too high as that the groundwater table could be detected by GPR (< 10 m). Traveltimes were transformed into depths and corrected by the capillary rise height of 13.5 cm. This has to be done as GPR does not detect the pressure height of the groundwater table, i.e. the level of a free water surface in a borehole, but is sensitive to the water content in the sediment. After this correction the depths correspond to pressure heads of a free groundwater table as can be measured at monitoring wells (Fig. 10). The GPR water tables fit well to the water levels in the observation wells that are dispersed in the area of investigation and regularly measured (see Fig. 3 in Sulzbacher et al., 2012). When taking into consideration all observation wells closer than 30 m to the GPR profiles and comparing the levels with GPR water tables, the rms deviation is 50 cm with maximal deviations of 80 cm found on top of the high dunes. The discrepancies can be explained by lateral variations of the groundwater table (most of the wells were not located directly on the profiles), temporal variations (the readings were not done at exactly the same time as the GPR survey but 1–2 months before), picking errors and uncertainties of the GPR data and an inaccurate velocity-depth model. Further, GPR can only detect the groundwater surface of unconfined aquifers, but does not measure pressure heads of confined aquifers that may be included in the observation-well readings. In the centre of the island, the groundwater table is found to be up to 3.5 m above sea level. On a large scale, it follows roughly the topography of the island, i.e. it is higher in the dune areas and sinks towards the coastal line and the lower marshland as in the western part of the area. Local depressions can be seen in the area of a deep dune valley with a confined aquifer (349750E/5962500N) and particularly around the pumping stations of the local water supplier, the position of which are also marked in Fig. 10. The situation is similar to the findings of Tronicke et al. (1999) who investigated the freshwater

HESSD
9, 3691–3720, 2012

lens of Spiekeroog, another East Frisian barrier island. They found the water table to be more than 1.5 m a.s.l. in the centre of this island and they observed lower water tables in the area of water production wells. However, the geology of this island is different to Borkum. Spiekeroog is characterised by Quarternary sands which are underlain by a Tertiary clay layer at 40–60 m that is assumed to be a barrier to the water in the upper sand deposits.

From the GPR groundwater tables, the thickness of the freshwater lens can be deduced by using the Herzberg-Ghyben relation (Eq. 1). In the region of the "CLIWAT 2"-drilling (see Fig. 10), the height of the groundwater table is found to be 1.5 m a.s.l., which results in a 61.5 m thick freshwater lens. This is in good accordance to the findings of ERT measurements in the vertical electrode chain that has been installed in the borehole and shows a strong increase of the electric conductivity between 48 and 61 m depths (Grinat et al., 2010). At the highest elevation of the groundwater table of 3.5 m a.s.l. in the central dune area, the equation predicts a 143.5 m thick freshwater lens. However, one has to consider that the relation is only a simple description and does not take into account a complex geology, varying salt concentrations in the subsurface and cannot describe non-stationary conditions. Numerical simulations have shown that the freshwater table is not that deep than predicted by the simple Herzberg–Ghyben equation (Sulzbacher et al., 2012).

5 Conclusions and outlook

We used GPR to investigate the shape of the eastern freshwater lens on Borkum island and to reveal hydraulically relevant subsurface structures. CMP and VRP measurements were used to deduce radar velocities in the subsurface. A simple velocity model with $v = 0.124\,\mathrm{m\,ns^{-1}}$ above the groundwater table and $0.065\,\mathrm{m\,ns^{-1}}$ below showed to be appropriate. From these velocities the porosity of the dune sediment was derived as well as the water content in the unsaturated zone. The velocity model was also used to transform the traveltimes of the CO data into depths. The low frequency data show

HESSD
9, 3691–3720, 2012

a sharper reflection at the groundwater table than the high frequency data, which is interpreted as an effect of the transition zone above the groundwater table. The derived groundwater tables are in good accordance to the observations at the monitoring wells in the area. Despite the topography of the island with up to 17 m high dunes on the GPR profiles, the deviation is small. In the centre of the island, groundwater table is found to be up to 3.5 m above sea level and it sinks down to sea level towards the coast line. Local depressions are observed in the region of a deep dune valley and around the pumping stations of the local water supplier.

GPR gives also valuable insights in the sediment structures and can map hydraulically significant layers, particularly if combined with boreholes. Highly permeable aeolian dune sediments could be distinguished from less permeable marine sediments by their inner structure. A hydraulically-tight silt loam layer was detected. This layer that was interpreted as a former tidal flat surface could be further characterised with GPR revealing erosion channels, so that hydraulically it acts an aquiclude with some limited leakage.

An interesting feature can be seen in Figs. 5 and 6: in the centre part of the profile, a weak blurry reflection can be recognised approx. 18 ns after the groundwater reflection, i.e. 0.3 m below the groundwater table. To the sides of the profile it is not visible as it is probably superimposed by sedimentologic reflections. This weak reflection is not a multiple reflection as it does not follow topography. Instead it is more or less parallel to the groundwater reflection and might be caused by grain-coating iron minerals. These minerals can typically be found in the groundwater fluctuation zone that is characterised by changing redox potentials and shows brown-yellow colours (Fig. 7). In the permanently saturated zone with reducing environment, the colour of the sand is grey, i.e. the grains have no significant iron-mineral coating. As grain-coating iron minerals have an impact on the dielectric properties of quartz (Josh et al., 2011), radar properties change at this interface and may cause a reflection. If so, it will be possible to reveal past groundwater fluctuations by GPR under certain conditions. However, this

HESSD
9, 3691–3720, 2012

hypothesis needs to be tested, e.g. by analysing the dielectric and chemical properties of undisturbed sand samples.

GPR data along measuring profiles were collected in a larger area ($\approx 6\,km^2$) in only a few days. As the effort of such investigations is acceptable, repeated surveys could be done over a longer period. This will give detailed information how the surface of the freshwater lens behaves with time. Furthermore, point information from monitoring wells can be extrapolated to larger areas. The absolute accuracy is lower than light plummet readings but GPR provides densely sampled data along the profiles. Geostatistical analysis showed that the small-scale variability of the groundwater table is high and the correlation length smaller than the distance in between the GPR profiles. This valuable information cannot be deduced from the readings of a few observation wells only. An interpolation in between the profiles or extrapolation to the whole area will cause large kriging errors and give an erroneous map neglecting the small-scale variability and providing only a trend on a large scale. If small-scale variation is of interest, a denser measuring grid is needed. This can easily be realised but depends on the terrain and will be more time consuming.

Combined interpretation or inversion of different geophysical techniques is promising for the future. A comparison of the top of the freshwater lens mapped by GPR with the saltwater-freshwater interface, as derived by airborne EM or ERT, can be used to evaluate the Herzberg-Ghyben relation. This will provide further information about the properties of the whole aquifer and can be used to calibrate and improve groundwater models. A combination of GPR and MRS may be used to characterise the hydraulic properties of sediments as both techniques are sensitive to differently bound water.

Acknowledgements. The authors would like to thank Dieter Epping, Raphael Holland, and Detlef Vogel for assisting the GPR measurements, the student Matthias Singer for assisting the core pile drillings and the municipal water supplier of Borkum for logistically supporting the field campaign. We like to acknowledge Cornelia Müller and Matthias Halisch for the pycnometer measurements, Franz Binot for his hints concerning geology, and Sebastian Winter for providing the data of the monitoring wells and his hydrogeological advice while planing the GPR investigations. Thanks to Markus Loewer for proof-reading the manuscript.

HESSD
9, 3691–3720, 2012

References

Ad-hoc-AG Boden: Bodenkundliche Kartieranleitung, 5 edn., Hannover, Germany, 2005. 3702

Annan, A. P.: Ground penetrating radar, in: Near Surface Geophysics, Vol. 13 of Investigations in Geophysics, Society of Exploration Geophysics, Tulsa, OK, 357–438, 2005. 3695

Bennett, M. R., Cassidy, N. J., and Pile, J.: Internal structure of a barrier beach as revealed by ground penetrating radar (GPR): Chesil beach, UK, Geomorphology, 104, 218–229, 2009. 3694

Bristow, C., Bailey, S., and Lancaster, N.: The sedimentary structure on linear sand dunes, Nature, 406, 56–59, 2000. 3694

Cassiani, G., Fusi, N., Susanni, D., and Deiana, R.: Vertical radar profiling for the assessment of landfill capping effectiveness, Near Surf. Geophys., 6, 133–142, 2008. 3697

Clement, W. P. and Knoll, M. D.: Traveltime inversion of vertical radar profiles, Geophysics, 71, K67–K76, 2006. 3698

van Dam, R.: Landform characterization using geophysics – recent advantages, applications, and emerging tools, Geomorphology, 137, 57–73, 2012. 3694

Dix, C. H.: Seismic velocities from surface measurements, Geophysics, 20, 68–86, 1955. 3696

Doolittle, J. A., Jenkinson, B., Hopkins, D., Ulmer, M., and Tuttle, W.: Hydropedological investigations with ground-penetrating radar (GPR): estimating water-table depths and local ground-water flow pattern in areas of coarse-textured soils, Geoderma, 131, 317–329, 2006. 3694

Ernst, J. R., Green, A. G., Maurer, H., and Holliger, K.: Application of a new 2D time-domain full-waveform inversion scheme to crosshole radar data, Geophysics, 72, J53–J64, 2007. 3697

Grinat, M., Südekum, W., Epping, D., Grelle, T., and Meyer, R.: An automated electrical resistivity tomography system to monitor the freshwater/saltwater zone on a North Sea Island, in: Ext. Abstr., Near Surface 2010, 16th European Meeting of Environmental and Engineering Geophysics, Zürich, 6–8 September 2010, 2010. 3693, 3705

Günther, T. and Müller-Petke, M.: Hydraulic properties at the North Sea island Borkum derived from joint inversion of magnetic resonance and electrical resistivity soundings, Hydrol. Earth Syst. Sci. Discuss., 9, 2797–2829, doi:10.5194/hessd-9-2797-2012, 2012. 3693

Harari, Z.: Ground-penetrating radar (GPR) for imaging stratigraphic features and groundwater in sand dunes, J. Appl. Geophys., 36, 43–52, 1996. 3694, 3703

HESSD
9, 3691–3720, 2012

Hardage, B. A.: Vertical Seismic Profiling: Principles, Handbook of Geophysical Exploration, Seismic exploration, 3 edn., 14, Elsevier, Amsterdam, 2000. 3697
Herzberg, B.: Die Wasserversorgung einiger Nordseebäder, J. Gasbeleucht. Wasserversorg., Berlin, 44, 815–819, 1901. 3693
Josh, M., Lintern, M. J., Kepic, A. W., and Verrall, M.: Impact of grain-coating iron minerals on dielectric response of quartz sand and implications for ground-penetrating radar, Geophysics, 76, J27–J34, 2011. 3706
Kaatze, U.: Complex permittivity of water as a function of frequency and temperature, J. Chem. Eng. Data, 34, 372–374, 1989. 3702
Keilhack, K. and Wildvang, D.: Bl. Borkum, Juist-West, Juist-Ost u. Norderney, vol. 914, 1010, 1011, 915, 916, 820, 821 of Erläuterungen zur Geologischen Karte von Preußen und benachbarten deutschen Ländern, Preußische Geologische Landesanstalt, Berlin, 1925. 3700
Klotzsche, A., van der Kruk, J., Meles, G. A., Doetsch, J., and Maurer, H., and Linde, N.: Full-waveform inversion of cross-hole ground-penetrating radar data to characterize a gravel aquifer close to the Thur River, Switzerland, Near Surf. Geophys., 8, 635–649, 2010. 3697
Kruse, S. E., Schneider, J. C., Inman, J. A., and Allen, J. A.: Ground penetrating radar imaging of the freshwater/saltwater interface on a carbonate island, Key Largo, Florida, Ext. Abstr., GPR 2000: the 8th International Conference on Ground Penetrating Radar; Goldcoast, 4084, 335–340, 2000. 3694
Møller, I. and Anthony, D.: A GPR study of sedimentary structures within a transgressive coastal barrier along the Danish North Sea coast, vol. 211 of Geol. Soc. London Spec. Publ., 55–65, 2003. 3694, 3702
Neal, A.: Ground-penetrating radar and its use in sedimentology: principles, problems and progress, Earth-Sci. Rev., 66, 261–330, 2004. 3694
Nielsen, L., Møller, I., Nielsen, L. H., Johannessen, P., Pejrup, M., Andersen, T. J., and Korshøj, J. S.: Integrating ground-penetrating radar and borehole data from a Wadden Sea barrier island, J. Appl. Geophys., 68, 47–59, 2009. 3694
Rejiba, F., Bobée, C., Maugis, P., and Camerlynck, C.: GPR imaging of a sand dune aquifer: a case study in the niayes ecoregion of Tanma, Senegal, J. Appl. Geophys., doi:10.1016/j.jappgeo.2011.09.015, in press, 2012. 3694
Sandmeier, K. J.: Reflex-Win Version 4.2, Windows 9x/NT/2000/XP/7-program for the processing of seismic, acoustic or electromagnetic reflection, refraction and transmission data, Sandmeier Scientific Software, available at: www.sandmeier-geo.de, Germany, 2011. 3700

HESSD
9, 3691–3720, 2012

Shen, L. C., Savre, W. C., Price, J. M., and Athavale, K.: Dielectric properties of reservoir rocks at ultra-high frequencies, Geophysics, 50, 692–704, 1985. 3695
Siemon, B., Christiansen, A., and Auken, E.: A review of helicopter-borne electromagnetic methods for groundwater exploration, Near Surf. Geophys., 7, 629–646, 2009. 3693
Sulzbacher, H., Wiederhold, H., Siemon, B., Grinat, M., Igel, J., Burschil, T., Günther, T., and Hinsby, K.: Numerical modelling of climate change impacts on freshwater lenses on the North Sea Island of Borkum, Hydrol. Earth Syst. Sci. Discuss., 9, 3473–3525, doi:10.5194/hessd-9-3473-2012, 2012. 3694, 3703, 3704, 3705
Topp, G. C., Davis, J. L., and Annan, A. P.: Electromagnetic determination of soil water content: measurements in coaxial transmission lines, Water Resour. Res., 16, 574–582, 1980. 3695
Tronicke, J. and Knoll, M. D.: Vertical radar profiling: influence of survey geometry on first-arrival traveltimes and amplitudes, J. Appl. Geophys., 57, 179–191, 2005. 3697, 3698
Tronicke, J., Blindow, N., Groß, R., and Lange, M. A.: Joint application of the surface electrical resistivity- and GPR-measurements for groundwater exploration on the island of Spiekeroog – Northern Germany, J. Hydrol., 223, 44–53, 1999. 3694, 3704
Tronicke, J., Holliger, K., Barrash, W., and Knoll, M.: Multivariate analysis of cross-hole georadar velocity and attenuation tomograms for aquifer zonation, Water Resour. Res., 40, W01519, doi:10.1029/2003WR002031, 2004. 3697
Yilmaz, Ö.: Seismic data analysis: processing, inversion, and interpretation of seismic data, Soc. of Explorat. Geophys., Tulsa, OK, 2001. 3696

HESSD
9, 3691–3720, 2012

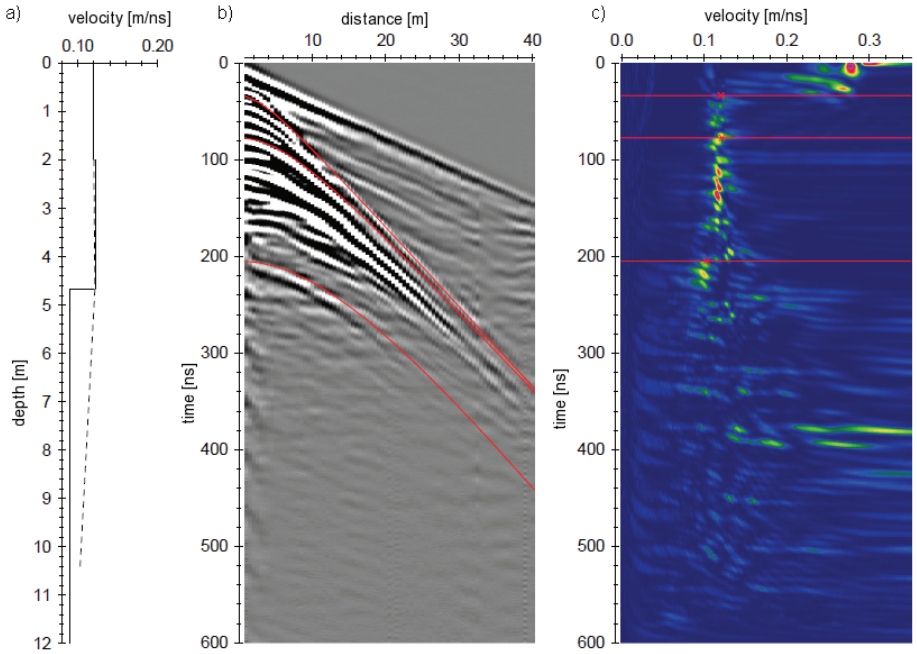

Fig. 1. CMP (80 MHz centre frequency) on top of a dune **(b)**, semblance analysis velocity **(c)** and deduced velocity model **(a)**.

HESSD
9, 3691–3720, 2012

GPR insight into the freshwater lens of Borkum island

J. Igel et al.

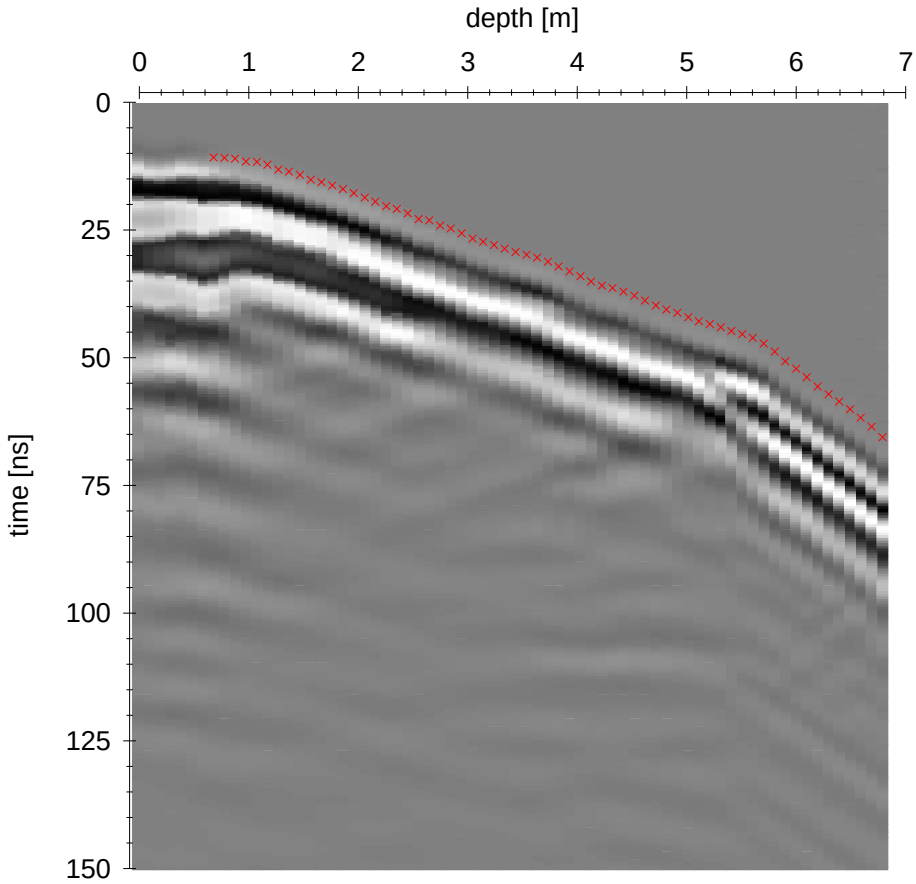

Fig. 2. VRP radar section in a monitoring well on top of a dune (100 MHz nominal frequency) with 1.0 m antenna offset from the well and picked arrival times. The amplitude of each trace is normalised in the plot.

HESSD
9, 3691–3720, 2012

GPR insight into the freshwater lens of Borkum island

J. Igel et al.

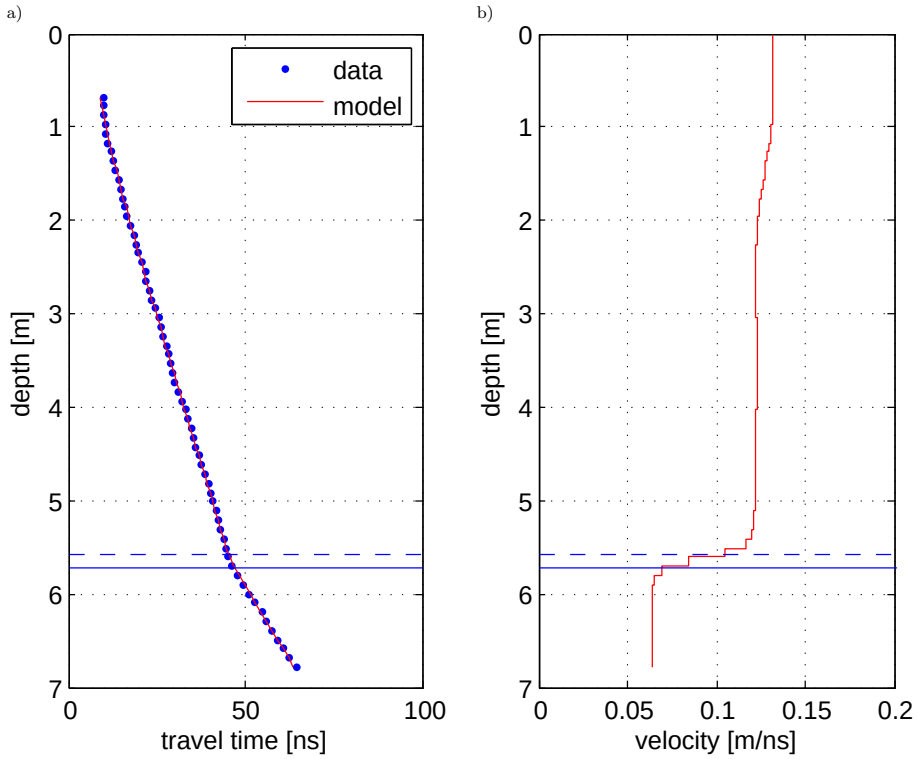

Fig. 3. Inversion of VRP data: picked traveltimes **(a)** and inverted velocity-depth model **(b)**. The groundwater level in the well is shown as solid blue line and the top of the capillary fringe as dashed line.

HESSD
9, 3691–3720, 2012

GPR insight into the freshwater lens of Borkum island

J. Igel et al.

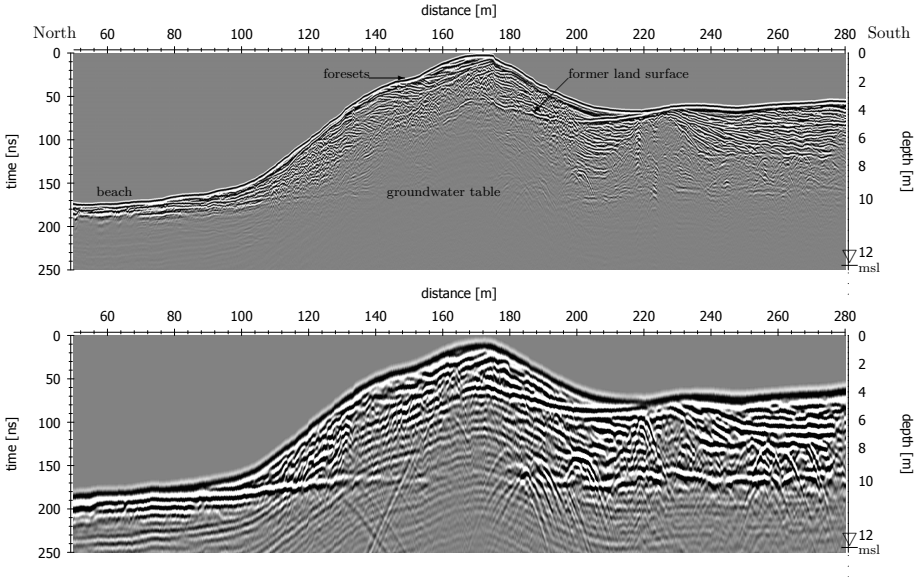

Fig. 4. GPR profile 1 (see Fig. 10 for location) from the North Sea over the main dune in direction of the inner island: 200 MHz (top), 80 MHz (bottom). The data are topographically corrected with the velocity of the unsaturated sand and the depths are calculated assuming a velocity of 0.124 m ns^{-1} above 9.6 m and 0.065 m ns^{-1} below. The amplitudes of both sections are normalised for comparison.

HESSD
9, 3691–3720, 2012

GPR insight into the freshwater lens of Borkum island

J. Igel et al.

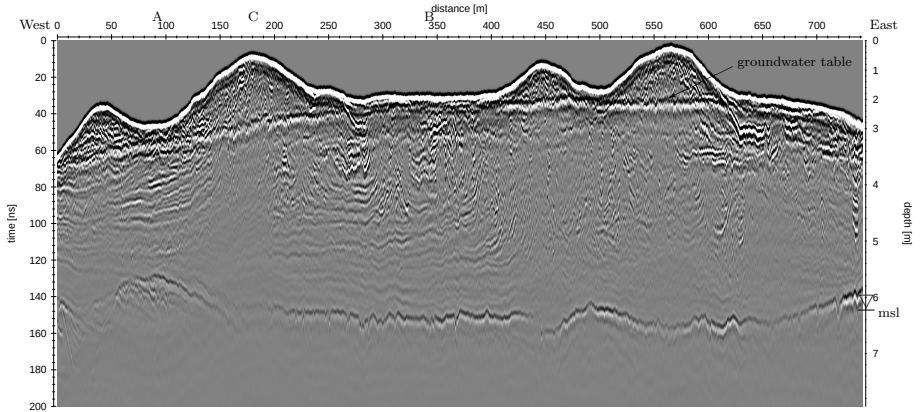

Fig. 5. GPR profile 2 (see Fig. 10 for location), 200 MHz. The data are topographically corrected with the velocity of the unsaturated sand. Depths are calculated assuming a velocity of 0.124 m ns^{-1} above 3 m and 0.065 m ns^{-1} below. The position of the 3 drillings are tagged on the x-axis.

HESSD
9, 3691–3720, 2012

GPR insight into the freshwater lens of Borkum island

J. Igel et al.

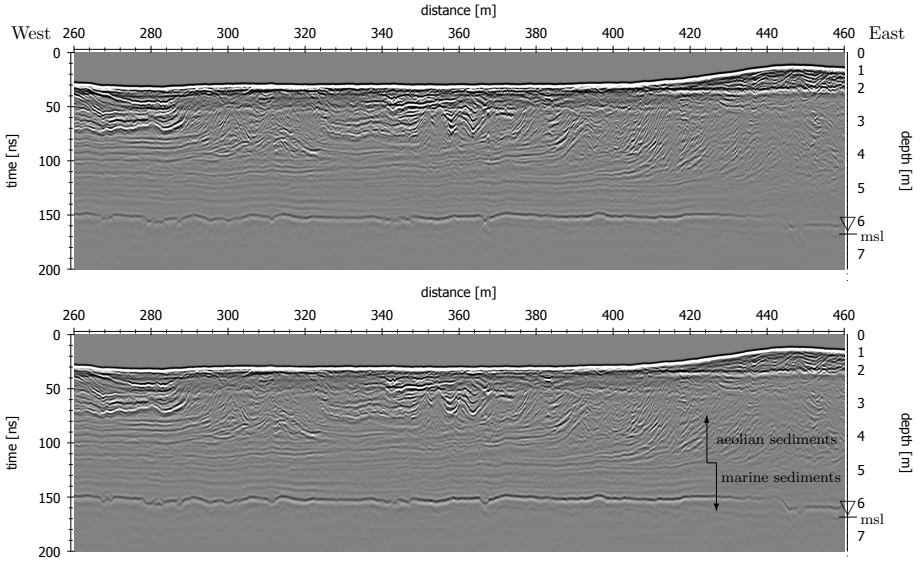

Fig. 6. Detail of GPR profile 2, 200 MHz (Fig. 5). Unmigrated data (top) and migrated data (bottom).

HESSD
9, 3691–3720, 2012

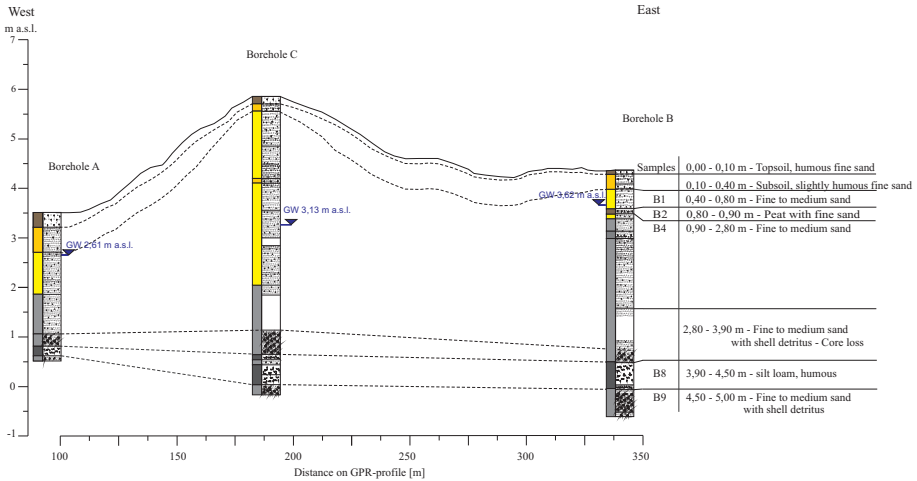

Fig. 7. Lithology of the drillings and geological model. The vertical scale is superelevated and the x-coordinates correspond to the x-axis of the radar sections Figs. 5 and 6. The depths where core loss appeared are in plain white. The sediment colouring is shown besides lithology as well as the groundwater tables. Samples at different depths were taken from drilling B (B1–B9).

HESSD
9, 3691–3720, 2012

GPR insight into the freshwater lens of Borkum island

J. Igel et al.

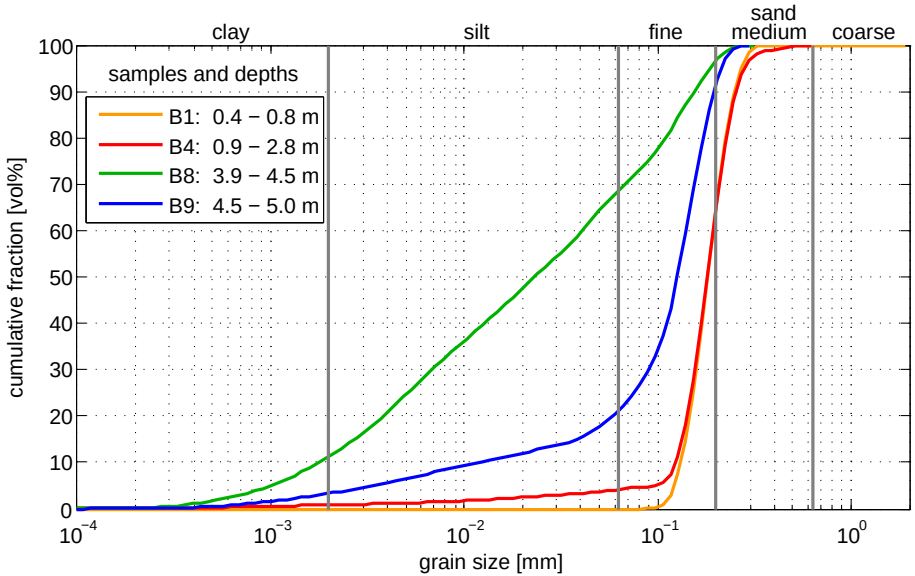

Fig. 8. Grain-size analysis of the samples from borehole B.

HESSD
9, 3691–3720, 2012

GPR insight into the freshwater lens of Borkum island

J. Igel et al.

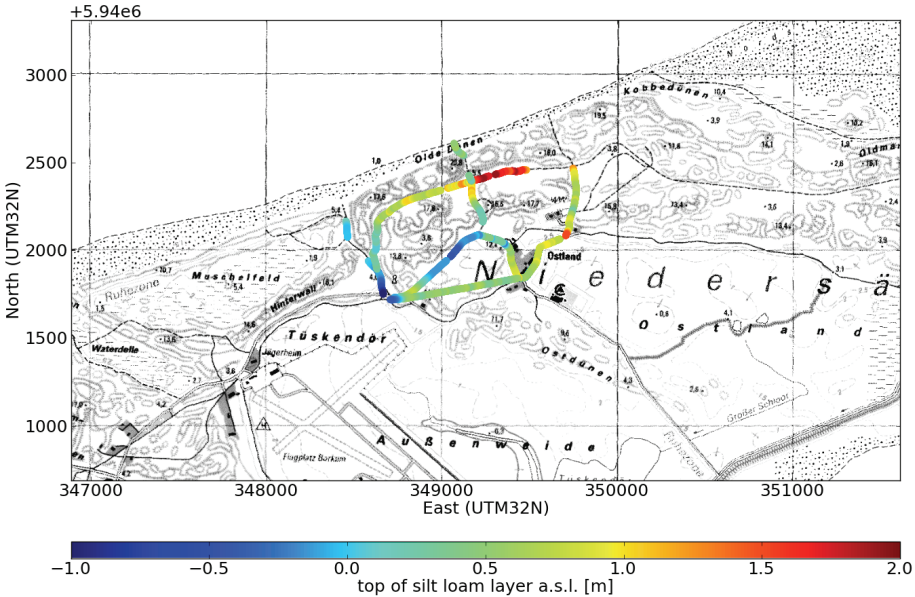

Fig. 9. Top of the silt loam layer where clearly visible in GPR data.

HESSD
9, 3691–3720, 2012

GPR insight into the freshwater lens of Borkum island

J. Igel et al.

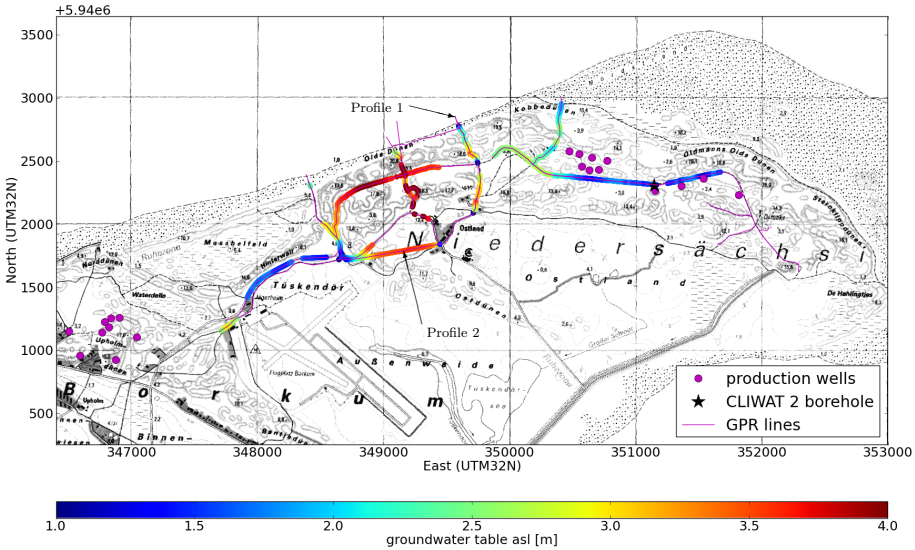

Fig. 10. Watertable of the freshwater lens in the eastern part of the island due to GPR measurements. The production wells of the local water supplier and the deep drilling "CLIWAT 2" are also plotted.

HESSD
9, 3691–3720, 2012